Wear xxx (xxxx) xxx

Contents lists available at ScienceDirect

Wear

journal homepage: www.elsevier.com/locate/wear

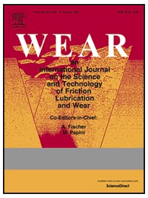

Electrostatic sensing of wear and friction dynamics in dry and starved-lubricated tribocontacts

Zaihao Tian [a,*], Ping Lu [a], Jo Grundy [b], Honor Powrie [c,a], Terence Harvey [a], Robert Wood [a]

[a] National Centre for Advanced Tribology, University of Southampton, Southampton, SO17 1BJ, UK
[b] Department of Electronics and Computer Science, University of Southampton, Southampton, SO17 1BJ, UK
[c] GE Aerospace, Eastleigh, SO53 4YG, UK

A R T I C L E I N F O

Keywords:
Oxidational wear
Electrostatic sensing
Friction
Starved-lubrication
Outlier detection

A B S T R A C T

Wear mechanisms in dry and starved-lubricated contacts are critical factors contributing to the degradation of component surfaces. Real-time monitoring of wear progression presents significant challenges due to the complex nature of these mechanisms and the varying conditions under which they occur. Electrostatic sensing offers a way of monitoring wear progression as it is correlated with surface charging from wear debris, contact potential differences associated with surface films, material phase transformations and wear transitions as well as from additive adsorption. This research employs two types of electrostatic wear sensor: a bar sensor for in-situ monitoring of wear progression and an array sensor for charge mapping of the resultant wear mechanisms in the scar.

Two sliding wear tests with tool steel against bearing steel are presented. Tests were conducted under dry sliding conditions or partially lubricated. Positive charge signals were detected for oxidational wear under dry contact conditions. Elemental mapping confirmed a patchy oxide film had developed and loose oxide wear debris became charged. Correlation is seen between surface charge maps and the patchy surface oxide films. A correlation was also found between the coefficient of friction and electrostatic charge, highlighting the potential of electrostatic sensors in detecting changing friction and wear levels. Negative charge signals were observed under starved sliding conditions using polyalphaolefin (PAO), primarily attributed to the degradation of PAO under high shear rates and tribo-charge mechanism. The charge progressively changed towards a more positive value, suggesting the progression of mild oxidational wear. Only very mild wear was measured at the end of the test (i.e. plastic flow of asperity material into valleys).

A map of real-time wear progression and measurement of instantaneous wear rate of oxidational wear and mild wear induced by partially lubricated contacts are presented. This advancement could significantly impact digital tribology, as the electrostatic sensing allows the surface chemistry to be better characterised. This allows for monitoring of the wear processes in action, allowing for better optimisation of predictive maintenance, as the information is real-time and the sensor is non-invasive.

1. Introduction

Understanding complex wear mechanisms is essential for maintaining the performance and longevity of mechanical components. Particularly challenging environments characterised by dry and starved-lubricated conditions, which are commonly encountered in high-stress mechanical systems, pose significant wear management difficulties. In dry contact scenarios, direct metal-to-metal contact leads to increased friction and elevated temperatures, fostering oxidational wear and abrasive wear where hard particles abrade the surfaces [1–5]. Starved-lubricated conditions, which feature fluctuating lubricant availability, can increase the thermal effects in the contacts, lead to scuffing-type failures and shorten fatigue life [6,7]. Even though some lubricant is present, it fails to maintain a continuous film, resulting in

---

This article is part of a special issue entitled: WOM2025 published in Wear.

[*] Corresponding author.
E-mail address: Zaihao.Tian@soton.ac.uk (Z. Tian).

https://doi.org/10.1016/j.wear.2025.205775
Received 10 September 2024; Received in revised form 26 November 2024; Accepted 13 December 2024
Available online 31 January 2025
0043-1648/© 2025 The Authors. Published by Elsevier B.V. This is an open access article under the CC BY license (http://creativecommons.org/licenses/by/4.0/).

Please cite this article as: Zaihao Tian et al., *Wear*, https://doi.org/10.1016/j.wear.2025.205775

intermittent breakdowns that mimic dry and boundary lubrication characteristics. Lubricant degradation due to high shear rates and thermal effects is also likely and this reduces the effectiveness in preventing wear [8].

With the trend toward more compact mechanical systems operating at higher power densities, effective wear monitoring is crucial for predicting wear patterns and preventing premature failures due to material degradation. The advent of low-cost sensing and data acquisition technologies has made real-time sensing of tribological parameters increasingly feasible [9]. Traditional monitoring techniques, such as piezoelectric, acoustic emission, ultrasonic, capacitive sensors, and thermocouples, are employed to detect features like power consumption, vibration, crack or corrosion propagation, wear debris, and lubricant temperature [10], which primarily serve as lagging indicators of wear. Consequently, these measurement methods are often inadequate for detecting subtle mechanistic changes during the early stages of contact degradation.

Electrostatic monitoring offers a significant advantage by measuring direct products of wear, rather than relying on secondary effects like increased vibration or temperature exceedance. Electrostatic measurements use a passive sensor connected to a charge amplifier to record voltage signals induced by changes in surface charge [11,12]. It has found broad applications in sectors like aero-engine gas path monitoring, lubrication oil wear debris detection, and bearing wear monitoring. The National Centre for Advanced Tribology at Southampton (nCATS) has conducted over 20 years research into electrostatic monitoring in tribological systems. The research includes detection of scuffing [13–16], diesel contaminants [17–19], bearing fatigue and pitting [20–25], wear debris [26,27], lubricant additives [18], oxidational wear [3,11,28], tribo-chemical wear [29–31], oil quality [32,33] and adhesive wear [34] using electrostatic monitoring. Recently work at nCATS has been exploring the possibility of detecting surface damage with a higher resolution, leading to the development of an electrostatic array sensor, which was used in the detection of oxidational wear [11].

Wear mechanisms that potentially generate electrostatic charge include surface chemistry changes, adhesive wear, abrasive wear, phase transformations, lubricant shearing, and wear debris etc [11]. This work focuses on surface wear which generates a contact potential difference (CPD) and tribo-charging mechanism caused by fluid shearing on the solid-fluid interface. CPD exists between two materials with different work functions when they are brought into thermal equilibrium [11,35]. The work function is demonstrated as an intrinsic parameter of a material's strength. A higher work function represents a more stable electronic state, which generates a higher resistance to changes in structure caused by mechanical and electrochemical actions [36]. Therefore it is a promising indicative parameter of a material's wear-resistance performance [37,38] and corrosion-resistance performance [39]. Apart from different materials, oxidised metal surfaces or surfaces with absorbed lubricant can also exhibit work functions that differ from the bulk material [11]. This difference in work function generates a CPD, which can be detected through electrostatic sensing. Tribo-charging occurs due to the relative motion between a fluid and a solid interface. At a solid-liquid interface, an electrical double layer naturally forms. Charge generation takes place when the fluid motion shears this double layer at the interface between the solid surface and the liquid phase. As a result, the liquid phase carries a portion of the electric charge from the double layer, generating free electrostatic charges. This mechanism is thought to be a potential charge source in lubricated wear processes due to the high shear nature of the tribocontact [32].

This work aims to investigate the dynamics of wear and friction in dry and starved-lubricated conditions, and their correlations with electrostatic charge. A bar sensor is employed to detect real-time charge and explore its correlation with wear progression and friction. Additionally, an array sensor is used to generate post-test charge maps, enabling the measurement of residual charge and the investigation of localised charge mechanisms. Machine learning techniques are applied to conduct an in-depth analysis of wear progression, facilitating the identification of early wear signs. This approach not only enhances machine efficiency but also reduces operational costs, representing a significant step toward the development of smart machines.

2. Material and methods

2.1. Materials

To investigate the wear mechanisms in dry and starved-lubricated conditions, two sets of sliding tests using rollers against plates were conducted using a TE77 reciprocating tribometer (Phoenix Tribology Ltd, Kingsclere, UK). The rollers, made of AISI 52100 steel, have a diameter of 6 mm and a length of 20 mm. The plates, made of BO1 BS4659 tool steel, have a length of 57.5 mm and a width of 25 mm. The plates used in the dry tests were lapped to achieve a surface roughness of Ra (average roughness) 0.173 ± 0.018 μm, while the plates used in the starved-lubricated tests had a surface roughness of Ra 0.052 ± 0.001 μm. The properties of the two steels are listed in Table 1. Before and after tests, the samples were ultrasonically cleaned with acetone for 5 min.

In the starved-lubricated tests, Polyalphaolefin (PAO) 4 oil (supplied by ExxonMobil Chemical, Baytown, Texas, US) was used. Its simplicity as a synthetic base oil facilitates a clearer understanding of the test results by minimising the influence of complex additive interactions. The properties of PAO 4 are detailed in Table 2. Starved-lubrication was achieved by applying a single drop of oil onto the plate and spreading it across the surface, resulting in an approximate quantity of 0.0015 g/cm^2.

2.2. Test conditions

The tests were conducted using a TE77 reciprocating tribometer. The tribometer setup includes a moving roller mounted in a reciprocating carrier which oscillates against a stationary plate as shown in Fig. 1. The TE77 is driven by a motor cam and scotch yoke assembly that delivers pure sinusoidal motion with a stroke length of 0.025 m. During the tests, stroke position, load, friction force, and electrostatic charge were continuously monitored. Both dry and starved-lubricated tests were performed at room temperature (~20 °C), with the test conditions summarised in Table 3. In comparison to previous studies conducted under dry [3,28] and lubricated conditions [18] which employed maximum contact pressure of 1–2 GPa and sliding speed of 0.1–5 m/s, this work used lower-speed sliding (0.05–0.1 m/s) and reduced load corresponding to a maximum contact pressure of 0.08–0.22 GPa. These conditions were designed to induce wear at a lower rate, facilitating the investigation of the electrostatic sensors' responses to mild and early-stage wear, and also ensuring appropriate electronic responses and adequate data capture for each stroke.

Table 1
Properties and elemental composition of AISI 52100 and BO1 BS4659 steel [40,41].

Property/element	AISI 52100 steel (roller)	BO1 BS4659 tool steel (plate)
Density (kg/m^3)	7810	8000
Elastic modulus (GPa)	200	230
Poisson ratio	0.28	0.29
Hardness (HV)	848	800
Fe (%)	96–97	>96
C (%)	0.93–1.05	0.85–1
Mn (%)	0.25–0.45	1.1–1.35
Si (%)	0.15–0.35	<0.4
W (%)	–	0.4–0.6
Cr (%)	1.35–1.60	0.4–0.6
Ni (%)	~0.25	<0.4
Cu (%)	~0.30	<0.2
P (%)	~0.025	<0.035
S (%)	~0.015	<0.035

Table 2
Properties of PAO4 base oil.

Kinematic viscosity, cSt, 100 °C	Kinematic viscosity, cSt, 40 °C	Viscosity index	Flash point, °C	Specific gravity (15.6/15.6 °C)
3.8	16.8	124	>222	0.82

Dry-2 and Dry-3 had two and five runs respectively. Between the runs the plates were removed from the rig for charge map generation and surface observations. Starved-2, Starved-3, and Starved-4 had two, five, and twelve runs respectively, with the plates remaining fixed on the rig throughout the tests to minimise oil evaporation as much as possible. In the final run of Starved-4, the load was increased to 120 N to accelerate wear progression. The run was stopped immediately upon observing a marked rise in the coefficient of friction.

2.3. In-situ data collection on a reciprocating tribometer

As shown in Fig. 1, an electrostatic (ES) bar sensor was mounted on the reciprocating carrier to measure real-time electrostatic charge. The sensing element was positioned 0.4–0.45 mm away from and parallel to the plate surface, set using a feeler gauge, and the ES signal was amplified using a Brüel & Kjær 2635 charge amplifier with an amplification factor of 1V/pC. Stroke position and per stroke friction force were collected from the TE77 system, and ES signal were recorded at a sampling rate of 1 kHz.

2.4. Ex-situ measurements of samples

ES charge maps were generated using an ES array sensor immediately after the completion of the tests. Details of the array sensor and the process of creating the charge maps was introduced in Ref. [11].

After removing the loose wear debris using compressed air, the roughness of the samples was measured using a contact-based profilometer, Intra Touch (Taylor Hobson, Leicester, UK), which performed single 2D profile measurements with a vertical resolution of 4 nm and a stylus vertical range of 1 mm. The surface topography of the rollers and plates was measured using a high-resolution non-contact optical 3D surface measurement device, Alicona G4 Infinite-Focus profilometer (Alicona Imaging GmbH, Raaba, Austria). To investigate the wear mechanisms, a JEOL JSM-7200F scanning electron microscope (SEM) equipped with an EDAX EDS (Energy Dispersive X-Ray Spectroscopy) detector (JEOL Ltd., Tokyo, Japan) was used. After each runs in Dry-3, SEM/EDS analysis was conducted at twelve positions within the wear scar to investigate relationships between localised wear mechanisms and charge distribution.

3. Data processing and correlation

3.1. Signal processing

Before analysing the ES data, it is necessary to process the raw data, as it may exhibit slopes due to factors such as slight misalignment of the sensor or sample fixture, or shifts caused by the DC offset from the charge amplifier. For all tests, the ES data were processed following the procedure outlined in Fig. 2. The data were binned using a bin width of 0.2 mm to ensure consistency in data length. Multiple cycles at the beginning of each test (e.g., cycles 3–7) were selected to extract the slope of the signals, as minimal wear occurred during the initial cycles and the data were relatively smooth. This ensured that any slopes detected were more likely due to system factors. The data from these cycles were averaged, and a linear regression was performed on the averaged data within the wear scar region (0 mm–8 mm of the stroke) to determine the slope. Once the slope was determined, it was subtracted from each cycle of the ES data to correct for any tilts. Following the slope removal, a DC offset correction was performed. This correction was based on the data from the non-worn area of the sample (16 mm–17 mm of the stroke). For each cycle, the mean value of the data in this non-worn region was calculated and subtracted from the data over the entire stroke to eliminate any baseline shifts caused by the charge amplifier's DC offset.

For statistical analysis, friction data at the reversing points (from −12.5 mm to −11 mm and from 11 mm to 12.5 mm of the stroke) were excluded due to fluctuations caused by changes in sliding speed and direction. Only the central section, from −11 mm to 11 mm within each stroke, was taken into consideration. This approach ensured that the

Table 3
Conditions for dry and starved tests conducted at room temperature (~20 °C).

Test No	Sliding distance (m)	Load (N)	Reciprocating frequency (Hz)	Initial maximum contact pressure (GPa)
Dry-1	62.5	15	1	0.1
Dry-2	125(62.5 × 2)	10 and 15[*]	1	0.08
Dry-3	312.5 (62.5 × 5)	15	1	0.1
Starved-1	62.5	80	2	0.22
Starved-2	125 (62.5 × 2)	80	2	0.22
Starved-3	312.5 (62.5 × 5)	80	2	0.22
Starved-4	744.25 (62.5 × 11 + 56.75)	80 and 120[**]	2	0.22

[*] In 'Dry-2', the applied load was 10 N in the first 1250 strokes, and 15 N in the second 1250 strokes.

[**] In 'Starved-4', the applied load was 80 N in the 1250 × 11 strokes, and 120 N in the last 1135 strokes.

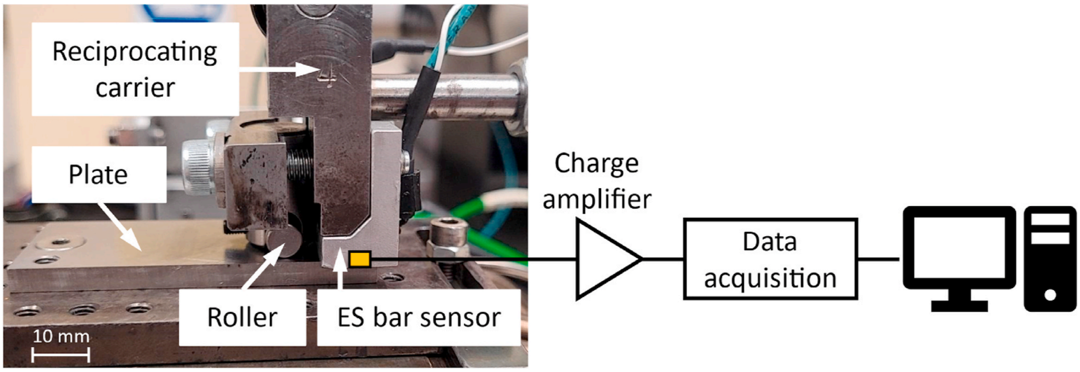

Fig. 1. Configuration of the roller-plate contact on TE77 and data acquisition system.

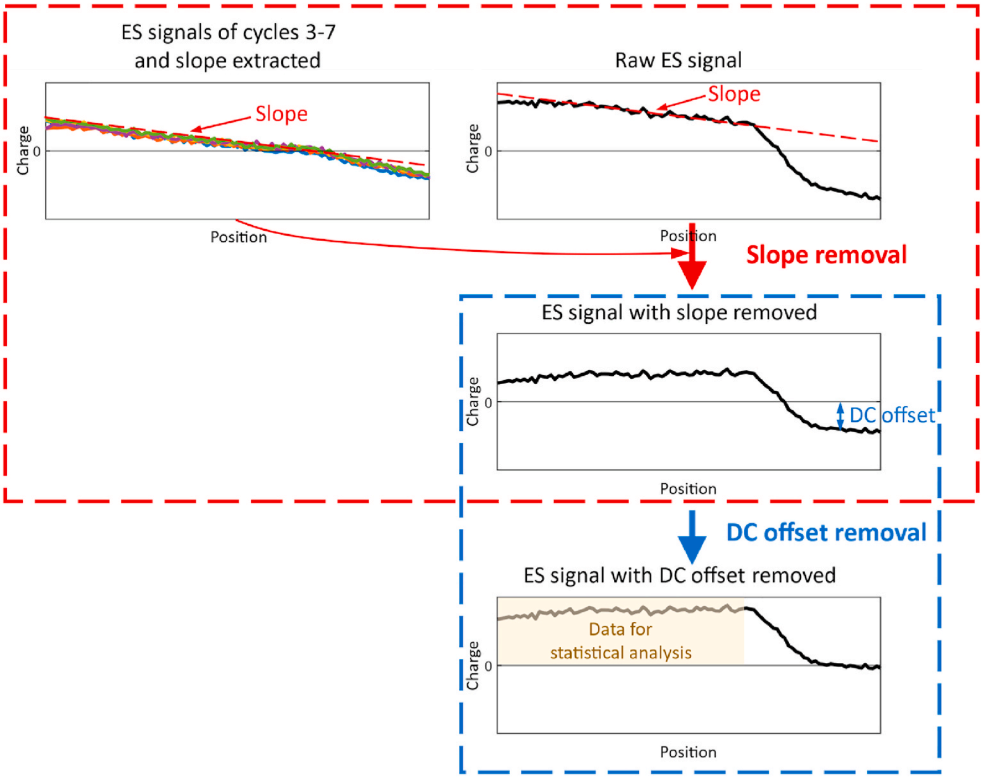

Fig. 2. Signal processing of ES data to remove slopes and DC offset.

analysis focused on the central part of the stroke, where both the ES and friction data were most relevant for understanding wear progression.

3.2. Data correlation

Correlation analysis was conducted to quantify the relationship between various statistical features of the Coefficient of Friction (CoF) and the ES bar sensor data collected during the tests. The statistical features considered include max, min, mean, standard deviation, RMS, skewness, and kurtosis. As presented in Ref. [11], CoF and ES both increased as oxidational wear progressed in the dry sliding test. In this work, the relationship between CoF and ES was assumed as linear and the Pearson correlation coefficient was calculated using MATLAB's `corr` function to evaluate the relationship. The correlation coefficients range from −1 to 1, where a value of 1 indicates a perfect positive linear relationship, −1 indicates a perfect negative linear relationship, and 0 indicates no linear relationship.

Correlation between localised ES signal and element concentration on the surface was also studied using charge maps generated by the ES array sensor and SEM/EDS maps. By comparing the statistical features, deeper insights into the wear progression were obtained. This approach enabled the identification of early evidence of contact decay from the surface charge maps, integrating elemental composition data to provide a comprehensive understanding of the wear mechanisms and their evolution over time.

3.3. Outlier detection

Previous work, in this and other fields suggests, that a good range of different outlier detection algorithms are successful in different tasks. In this work, five outlier detection algorithms were used, based on a mixture of traditional and deep learning approaches. The first one, Feature regression with L2 penalty (FRR) is based on feature-based regression. The features are each individually used as a target for regularised regression with all the other features used as input data. The error on each feature is added up to give an individual sample outlier score. The second, Isolation Forest (IF) is based on an ensemble of decision trees, where the number of divisions to isolate a data point is used as the outlier score [42]. Each division is made along a randomly chosen value in a randomly chosen dimension. The third algorithm is a one-class support vector machine (OCSVM) [43] which uses a support vector machine to characterise the density of the data, where the support vectors are those that surround the main density of the data, as defined by a tuneable parameter ν. The outlier score is the value of the coefficient on the support vector. The fourth method is based on a Long-Short Term Memory (LSTM) deep learning algorithm [44], which attempts to reconstruct the series, and the reconstruction errors are used as the outlier score. The fifth method is an autoencoder (AE) where by the data is squeezed though a multilayer perceptron with a smaller middle layer, and is trained to reconstruct the data [45]. The data points with larger reconstruction errors are more outlying, so this is used as the outlier score. All these algorithms and more are available easy to use Python package https://pypi.org/project/odds/.

To ensure reliability, as many of these algorithms are stochastic in nature, due to random network initialisation, and stochasticity in the backpropagation methods used to train these networks, the outlier score was calculated 32 times with each algorithm and the average was taken. OCSVM is deterministic, so will not vary. FRR will vary somewhat, as stochastic gradient descent is used in the solve, rather than the direct solution of the normal equation, due to the large quantity of data for this case. IF will vary, as random splits are used each time, and LSTM and AE, the deep learning methods will vary, averaging will ensure any random variations are removed.

4. Results and discussion

4.1. Dry sliding tests

This section discusses the friction, wear mechanisms, and ES charge during dry tests, with a particular focus on the results from Dry-3.

4.1.1. Evolution of oxidational wear and its interactions with friction

The CoF against sliding distance for the dry tests Dry-1, Dry-2, and Dry-3 is shown in Fig. 3. For each test, the plot was generated using mean values of CoF calculated over cycles with a length of 0.05 m. The same method was used to plot the ES data, as well as the CoF and ES data for the starved-lubricated tests. The CoF levels were comparable across the three tests, ranging from 0.2 to 0.6, with an increasing trend observed in each run. As discussed in Ref. [11] which presented Dry-2, the increase in friction was primarily due to the formation of oxide films on the surface, and Fe_3O_4 was the predominant oxide according to the value of CoF.

At the beginning of the second to fifth runs in Dry-3, the CoF was lower compared to the end of the previous run, this is probably due to the removal of hard wear debris during test stops when the plates were taken off the rig for charge map generation and surface observations. It is noted that in the first and third runs of Dry-3, there were periods when the CoF was noisy. This could be attributed to progression of abrasive wear which will be discussed later.

4.1.2. Wear mechanism and correlation with electrostatic charge

The evolution of the ES charge within the wear scar on plates during the dry tests Dry-1, Dry-2, and Dry-3 was detected by the ES bar sensor and is shown in Fig. 4. A positive charge was detected in all tests. As discussed in Ref. [11], the positive charge detected under dry sliding conditions indicated the presence of oxide, either as a film or as oxidised wear debris. The phenomenon was due to the higher work function of the oxide [46], which led to the material becoming positively charged when in contact with unoxidised steel.

It is observed that at the beginning of the second run of Dry-2, the charge level was lower than at the end of the first run. A similar pattern is noted in Dry-3, where the charge was lower at the start of the second to fifth runs compared to the end of the preceding runs. This reduction in charge can be attributed to charge relaxation during the pauses between tests. Given that the oxide exhibits semi-conducting behaviour, the charge relaxes gradually over time when the plates were connected to ground. The relationship between charge relaxation and the pause duration in Dry-2 and Dry-3 tests is illustrated in Fig. 5. It is evident that charge relaxation increased with longer pause durations. The pause durations varied because of the different accounts of time required to create charge maps and conduct optical and electron microscopy observations.

To investigate the wear mechanisms, optical and SEM observations of the wear scar were conducted. An optical image of the wear scar after the first run in Dry-3 is shown in Fig. 6 (a), and SEM images of twelve positions on the wear scar are shown in Fig. 6 (b). It is seen that in Fig. 6 (a), most of the wear scar had the steel colour and there were two black stripes where the surface was worn out. SEM images at positions 1, 2, 3, 7, 8, and 9, corresponding to the steel-colour areas, show the presence of oxide films on the plate surface, indicating the formation of oxidational wear. In contrast, SEM images at positions 4, 5, and 6 within the black stripes show a worn surface with scratches in the direction of sliding, which is recognised as abrasive wear. A comparison of the two wear mechanisms is evident in positions 10, 11, and 12, where a mixture of both is observed. Oxidational wear is observed on the left side, while abrasive wear is presented on the right side.

The evolution of the wear scar in Dry-3 is shown in Fig. 7 (a). After the first run (Dry-3-1), the abrasive wear area visible as black stripes constituted 31.7 % of the total wear area. This increased to 41.9 % after the second run (Dry-3-2) and eventually reached 100 % following the third run (Dry-3-3). Notable increases in the abrasive wear area during Dry-3-1 and Dry-3-3 corresponded to the noisy periods in the CoF observed in Fig. 3. As seen in Fig. 7 (b), oxide films were present in position 1 after Dry-3-2, with lapping scars still visible on the surface. By the end of Dry-3-3, abrasive wear had become dominant in this position, and most of the oxide films had been worn off. The ploughing and fracture mechanisms, along with the breakdown of oxide films, debris hardening and egress occurred during Dry-3-3 contributed to the deviations in the CoF.

To discuss the wear mechanisms in dry tests, Dry-2 is used as an example because both oxidational and abrasive wear were produced after the test. In Dry-3, both oxidative and abrasive wear were present on the wear scar during the first three runs as seen in Fig. 7; however, the roller was not removed from the rig for observation until the end of the test to maintain the continuity of the test. As a result, the wear scar on the roller was not observed until the test concluded, so a correlation between the wear on the roller and the plate could not be established. Observations of the wear scar on the plate and roller after Dry-2 are presented in Fig. 8.

As shown in Fig. 8 (a), both steel-colour areas and black stripes were present on the wear scar, corresponding to different wear mechanisms: oxidational wear (Fig. 8 (b)) and abrasive wear (Fig. 8 (c)) respectively. Corresponding to the abrasive wear area on the plates, grooves were also observed on the harder roller as presented in (Fig. 8 (d)). The SEM/EDS analysis of the wear debris from Dry-2 is shown in Fig. 9. The corresponding oxygen and iron maps reveal that the debris is composed of both oxide particles and metallic debris. The debris was likely to be strain hardened and thus harder than the roller and able to abrade it.

The Wear mechanism under dry condition is illustrated in Fig. 10. At a relatively low sliding speed (50 mm/s in this work), the oxide films formed on the plate surface due to oxidation process which was promoted by frictional heating and accumulation of oxide debris [1,2,47]. Fractured oxides and oxidised metallic wear particles can undergo strain hardening during sliding. These hardened particles then plough the surface, causing abrasive wear and generating additional oxide and metallic debris.

To investigate the relationship between charge and oxygen concentration on the wear scar of the five runs in Dry-3, charge maps were generated using data collected by the ES array sensor, and EDS analysis was conducted at twelve positions on the wear scar after each run. As an example, the charge map of the wear scar after the first run is shown in Fig. 11 (a), and the oxygen concentration at the twelve marked positions measured using EDS analysis is shown in Fig. 11 (b). The twelve positions correspond to those marked on the wear scar in Fig. 6 (a).

Correlation between localised charge and oxygen concentration in

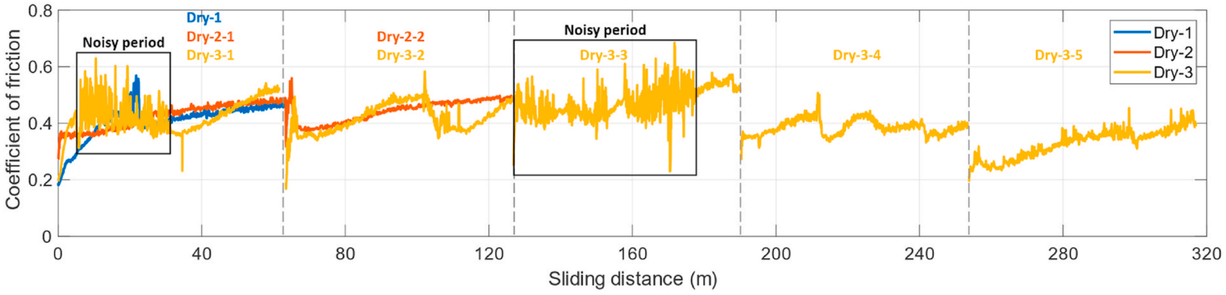

Fig. 3. CoF data in dry tests (Dry-1, Dry-2, and Dry-3).

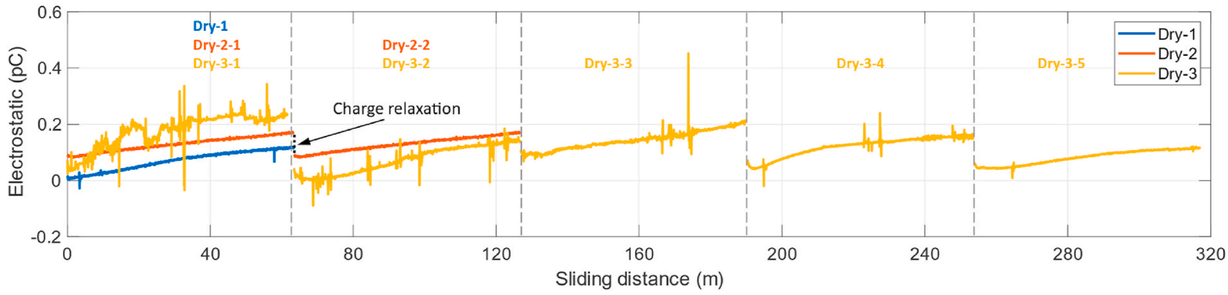

Fig. 4. ES bar sensor data in dry tests (Dry-1, Dry-2, and Dry-3).

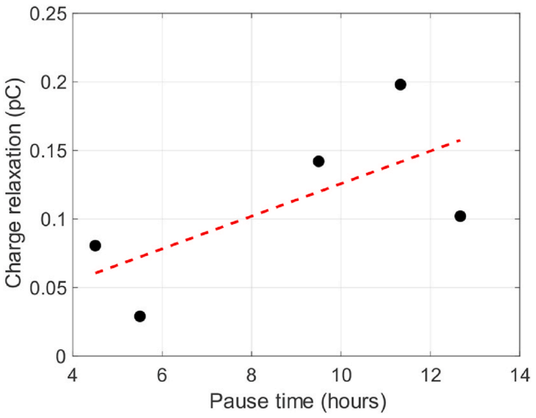

Fig. 5. Relationship between charge relaxation and stop time in Dry-2 and Dry-3.

the five runs of Dry-3 is shown in Fig. 12. The black dots are in oxidational wear regions, and the white dots are in abrasive wear regions. When considering the entire dataset, the correlation appears weak to non-existent. However, when analysed separately by surface characteristics, the charge and oxygen concentration exhibited a nearly linear relationship in the oxidational wear regions with a correlation coefficient of 0.79. In contrast, the abrasive wear regions showed little to no correlation. The weak correlation in the abrasive wear regions may be due to the removal of most oxide debris before SEM/EDS analysis, leading to oxygen concentration measurements that were not consistent with the conditions at the time of charge detection. Another reason could be that oxides with different compositions (oxygen content) were produced in the abrasive wear regions. Rapid reoxidation can occur on the nascent surfaces generated by abrasive wear, and the reformed oxide may differ in composition from the oxide films that develop under static conditions in the oxidational wear regions [1].

4.1.3. *Correlation between friction and charge*

The correlation analysis between the CoF and ES signals collected from the initial run of the Dry-2 test is illustrated in Fig. 13, using data from Ref. [11]. This test primarily induced oxidational wear. As depicted in the correlation matrix in in Fig. 13 (a), both the mean and root mean square (RMS) values of CoF and ES exhibit a strong positive linear relationship, with a correlation coefficient of approximately 0.979. Given that the charge can be either positive or negative, depending on the wear mechanisms involved, the use of mean values is more appropriate for this analysis. The cluster mapping of the CoF mean against the ES mean, shown in in Fig. 13 (b), further emphasises this relationship. The colour gradient in the cluster plot, ranging from blue (representing the start of the run) to red (representing the end of the run), demonstrates an increase in both friction and charge over the duration of the test. The same analytical approach was applied to other tests, revealing distinct correlation patterns corresponding to different wear

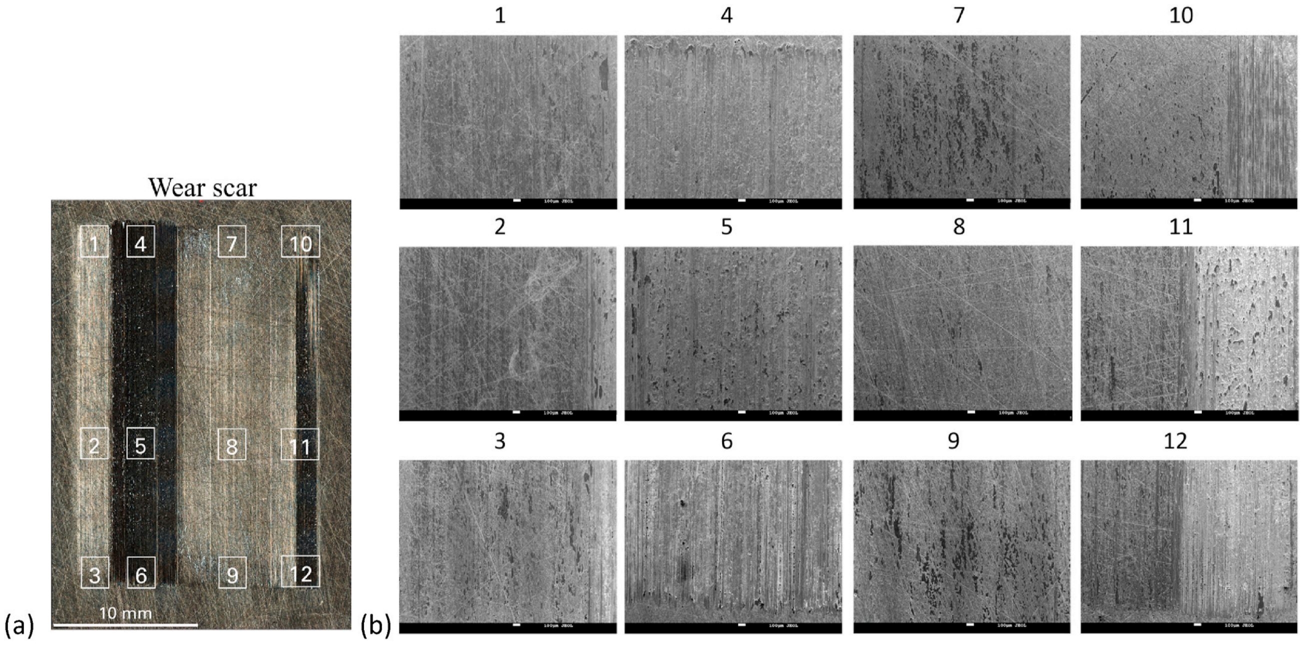

Fig. 6. (a) Optical image of wear scar on plate and (b) SEM images of wear distribution of the first run in Dry-3.

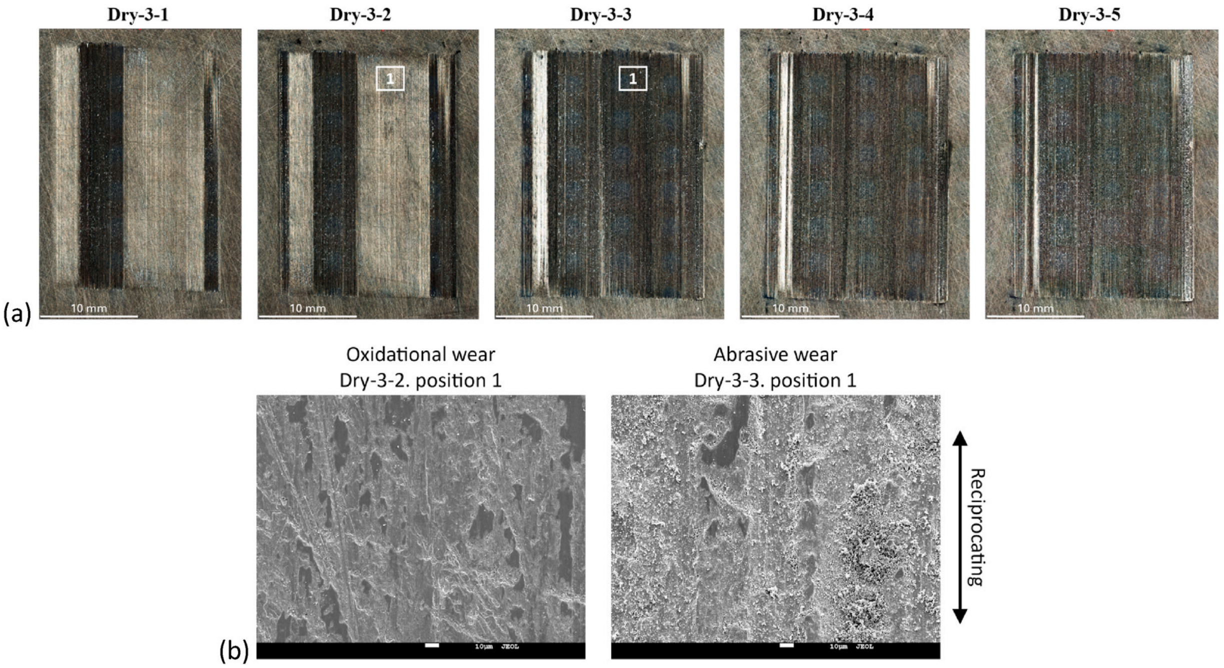

Fig. 7. (a) Evolution of wear scar in Dry-3; (b) transition from oxidational wear after Dry-3-2 to abrasive wear after Dry-3-3 in position 1.

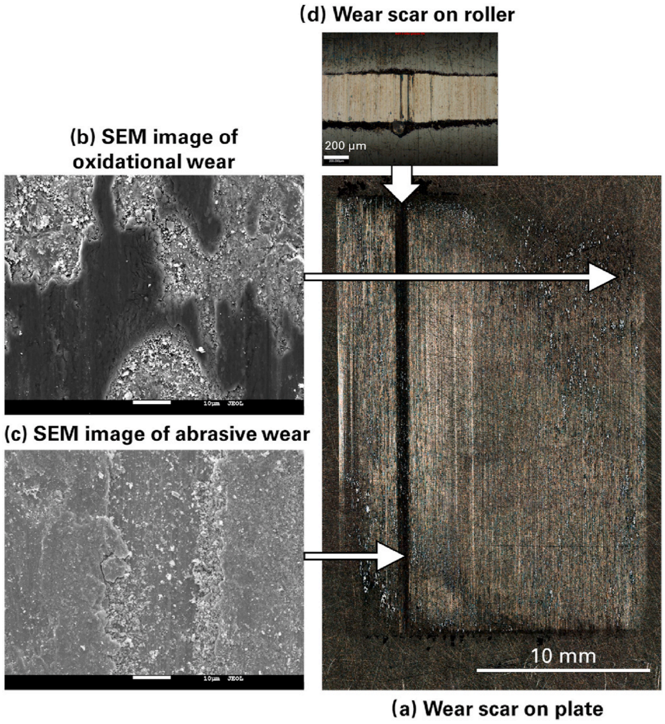

Fig. 8. (a) Optical image of wear scar on plate, (b) SEM image of oxidational wear, (c) SEM image of abrasive wear, and (d) optical image of wear scar on roller after Dry-2.

mechanisms.

The cluster mapping of the CoF mean against the ES mean for the first and final runs of the Dry-3 test is presented in Fig. 14. In the first run, as shown in Fig. 14 (a), the relationship was linear in some regions highlighted in the green circles, while nonlinear in others. As depicted in Fig. 6 (a), the wear scar after this run exhibited both oxidational and abrasive wear. As learnt from the Dry-2 test, the linear relationship corresponds to the dominance of oxidational wear, while the nonlinear relationship is associated with the progression of abrasive wear. In Fig. 14 (b), the relationship between ES and CoF in the final run appeared nearly linear, with a correlation coefficient of 0.927. This indicates a reduced progression rate of abrasive wear during this run, while the reemergence of a linear relationship suggests that oxidational wear once again became the dominant mechanism on the worn surface.

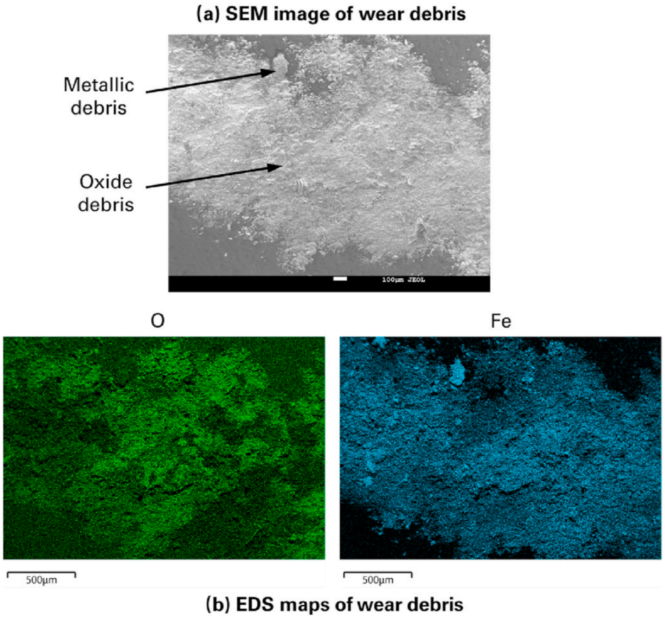

Fig. 9. (a) SEM image and (b) EDS maps (O and Fe) of wear debris after Dry-2.

In contrast to prior studies focused on oxidational wear at the final wear scar [4,5], this work employed friction and electrostatic charge monitoring at each cycle to track wear evolution and identify transitions between wear mechanisms in real time. Compared to earlier research [3, 28] that measured the net charge from the whole scar, this work achieved localised charge detection and established its relationship with wear mechanisms. Building on the study in Ref. [11], the relationship

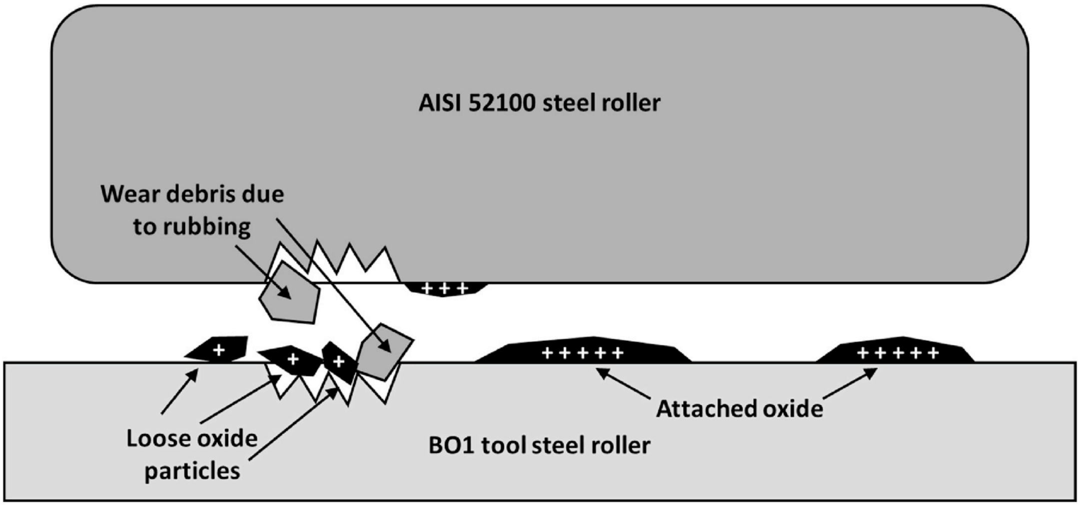

Fig. 10. Wear mechanism in dry sliding tests.

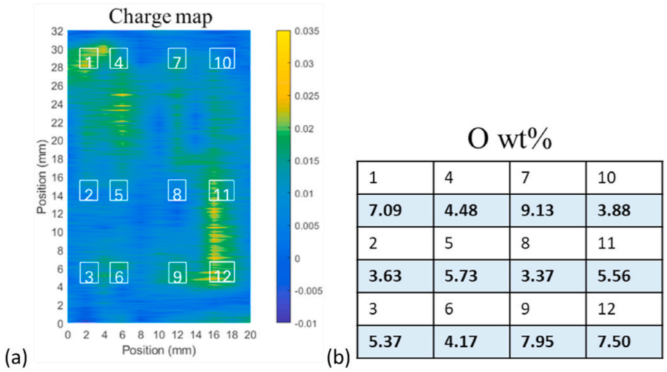

O wt%

1	4	7	10
7.09	**4.48**	**9.13**	**3.88**
2	5	8	11
3.63	**5.73**	**3.37**	**5.56**
3	6	9	12
5.37	**4.17**	**7.95**	**7.50**

Fig. 11. (a) Charge map generated by ES array sensor data, and (b) oxygen concentration distribution obtained by EDS analysis at twelve positions after the first run of Dry-3.

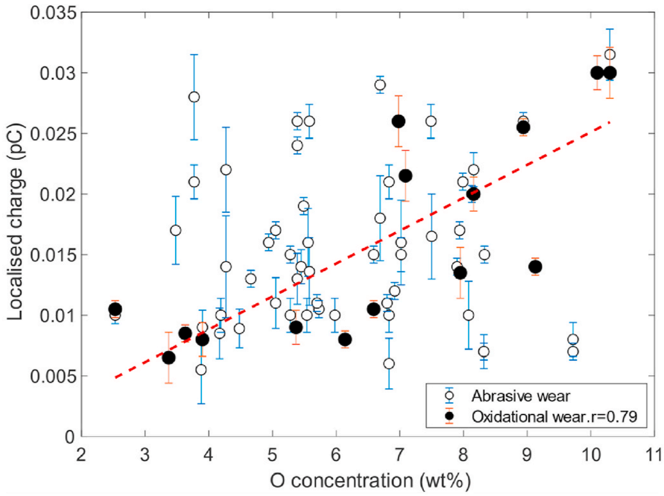

Fig. 12. Correlation between oxygen concentration and localised charge in test Dry-3.

between online electrostatic signals and friction was investigated, enabling the identification of wear mechanisms in real time. Additionally, more data were collected to validate the relationship between surface charge and oxide formation.

4.2. *Starved sliding tests*

4.2.1. *Wear mechanisms, friction and electrostatic charge*

The CoF versus sliding distance for the starved-lubricated tests Starved-1, Starved-2, and Starved-3 is shown in Fig. 15. The CoF was around 0.1 during the tests. As observed in the graph, there was a decrease in friction in Starved-1 and the first runs in Starved-2 and Starved-3. This could be attributed to the reduction in surface roughness of the plates during the running-in stage [48]. Roughness measurements of the plate tested in Starved-1 showed that the untested plate had a roughness average (Ra) of 0.052 ± 0.001 μm, a skewness (Rsk) of 0.042 ± 0.034, and a kurtosis (Rku) of 3.964 ± 0.391. In contrast, within the tested wear scar, Ra decreased to 0.046 ± 0.002 μm, Rsk to −0.383 ± 0.074, and Rku to 3.174 ± 0.178, indicating the removal of asperity peaks and the smoothing of the surface. The polishing of surface is also observed in the SEM images shown in Fig. 16. Compared with the untested surface shown in Fig. 16 (a), the lapping scars on the plates were polished off and no significant damage was observed in the post-test surfaces shown in Fig. 16 (b), (c), and (d).

4.2.2. *Charge correlated with lubricant shearing and degradation*

The evolution of the ES charge detected by the ES bar sensor during the starved tests (Starved-1, Starved-2, and Starved-3) is shown in Fig. 17. In all tests, the charge was negative and progressively shifted towards a more positive value, approaching zero, as the tests proceeded.

To investigate the charge mechanisms, SEM observations and corresponding EDS analysis were performed on the wear scars from the three starved-lubricated tests, with the results presented in Fig. 18. As the test duration increased, the accumulation of wear debris became more prominent, especially in the wear scar of Starved-3. This debris is believed to consist of oxidised particles, as evidenced by the elevated oxygen levels detected in this test, as indicated by the EDS spectrum.

Charge measurements on tribological surfaces under starved-lubricated conditions are affected by numerous factors, ranging from the lubricant type, the work function of the surfaces [34] to lubricant shearing. The lubricant type has been known to influence the magnitude and polarity of charge [49]. As investigated in Ref. [32], fully formulated synthetic oils tend to exhibit negative charge, while mineral base oils typically generate positive charge. In this study, synthetic oil was used, which could be a factor to the negative charge.

Lubricants complicate charge levels in that they absorb onto surfaces, with the absorbed molecules affect the work function [50]. Under sliding conditions, lubricants respond to shear, potentially altering bulk chemistry, undergoing thermal degradation, and interacting with the metal surface. Under starved-lubricated conditions, as the test

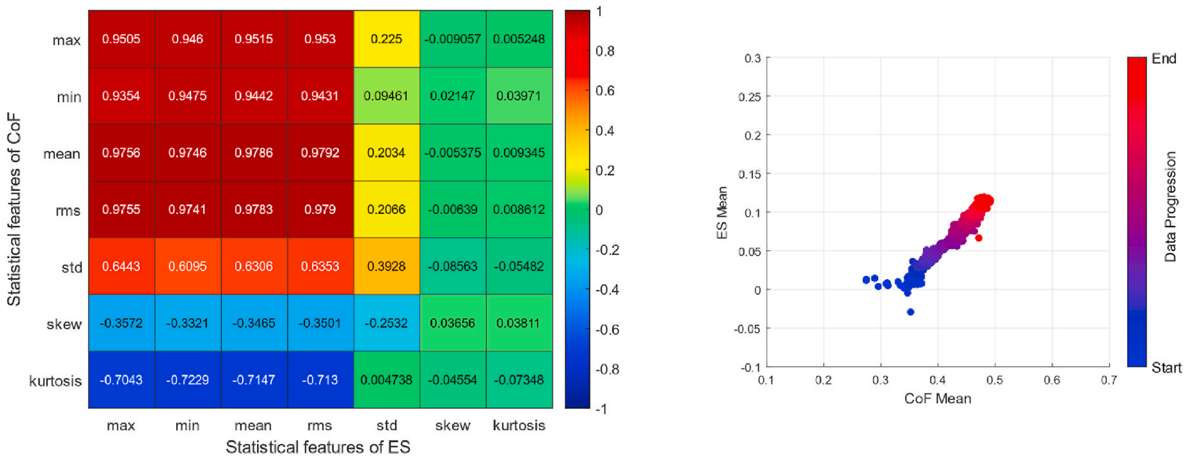

Statistical features of CoF \ Statistical features of ES	max	min	mean	rms	std	skew	kurtosis
max	0.9505	0.946	0.9515	0.953	0.225	-0.009057	0.005248
min	0.9354	0.9475	0.9442	0.9431	0.09461	0.02147	0.03971
mean	0.9756	0.9746	0.9786	0.9792	0.2034	-0.005375	0.009345
rms	0.9755	0.9741	0.9783	0.979	0.2066	-0.00639	0.008612
std	0.6443	0.6095	0.6306	0.6353	0.3928	-0.08563	-0.05482
skew	-0.3572	-0.3321	-0.3465	-0.3501	-0.2532	0.03656	0.03811
kurtosis	-0.7043	-0.7229	-0.7147	-0.713	0.004738	-0.04554	-0.07348

(a) (b)

Fig. 13. (a)Correlation matrix of statistical features between CoF and ES, and (b)cluster mapping of CoF mean against ES mean in the first run of Dry-2 test, based on data from [11].

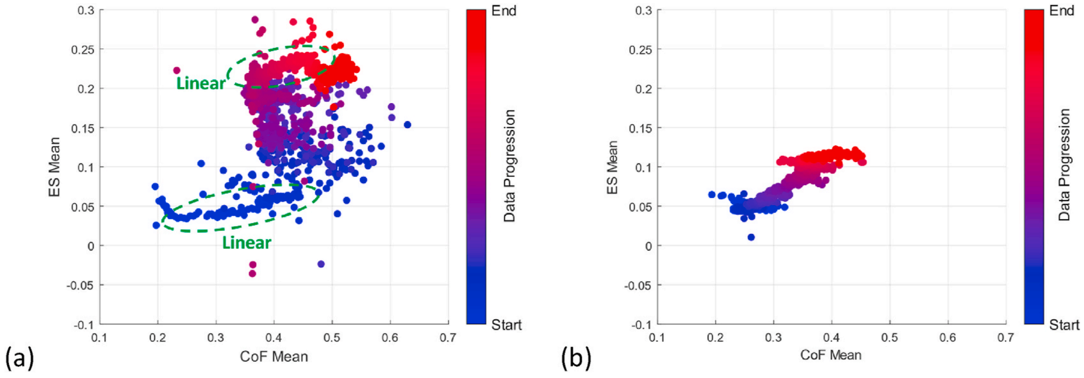

Fig. 14. Cluster mapping of CoF mean against ES mean in the (a) first run and (b) final run of Dry-3.

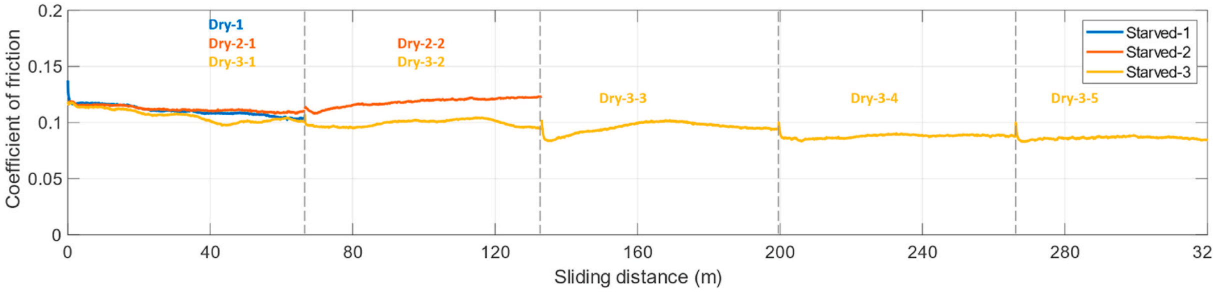

Fig. 15. Coefficient of friction versus sliding distance in starved tests (Starved-1, Starved-2, and Starved-3).

progressed, an increasing amount of lubricant was pushed out of the contact area, particularly towards the reversal points of the reciprocating motion. This allowed for metal-to-metal contact, which could result in a polishing effect, creating nascent surfaces that could interact with the adsorbed lubricant. The surface with absorbed lubricants can exhibit a different work function, resulting in a CPD with the untested surface and generation of a negative charge. Additionally, the negative charge may originate from the tribo-charging mechanism due to the relative motion of the double layer present at metal/oil interfaces [34].

As the lubricant was further removed, the contact area became increasingly starved, leading to partial dry sliding condition, where mild oxidational wear was likely to occur. Since oxidational wear induces a positive charge as discussed in Section 4.1.2, the near-zero charge observed at the end of Starved-3 could be attributed to this mild oxidational wear, as evidenced by the presence of wear debris as shown in Fig. 18.

In the starved tests, electrostatic charge and friction were not highly correlated because they were influenced by several different mechanisms. The charge was primarily generated from lubricant type, shearing, and CPD with untested surface, whereas the decrease in friction was attributed to the reduction in surface roughness.

4.3. Wear detection with outlier score analysis

Outlier detection was employed to identify abnormal events in the CoF and ES data during both dry and starved-lubricated tests, which may

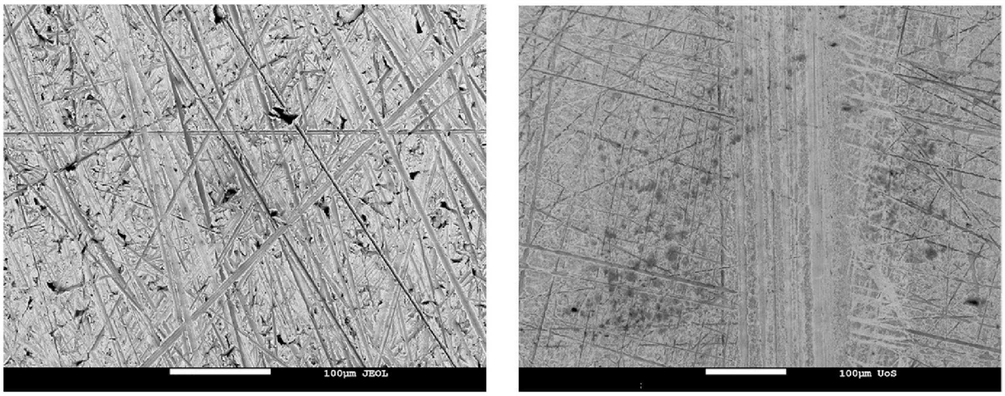

(a) Plate before test (b) Plate after Starved-1

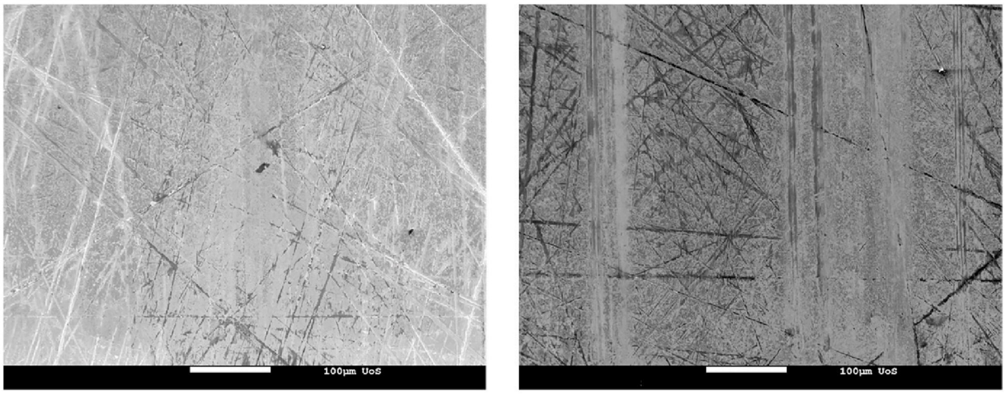

(c) Plate after Starved-2 (d) Plate after Starved-3

Fig. 16. SEM images of plates (a) before testing, (b) after Starved-1, (c) after Starved-2, and (d) after Starved-3.

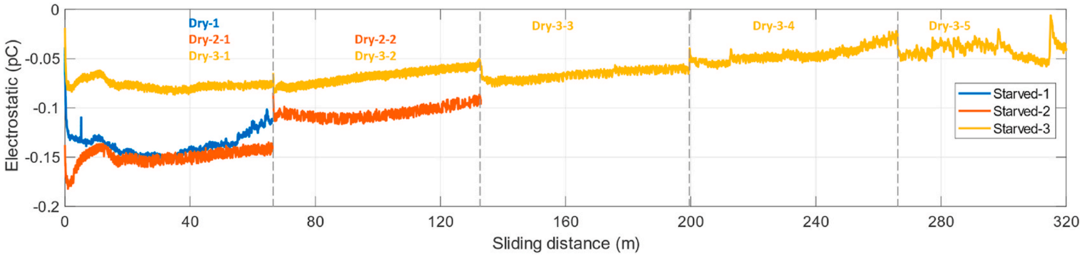

Fig. 17. Electrostatic bar sensor signal versus sliding distance in starved tests (Starved-1, Starved-2, and Starved-3).

provide insights into the initiation and progression of wear. As presented in Section 3.3, five outlier detection algorithms, FRR, IF, OCSVM, LSTM, and AE, were applied for normalised outlier score calculations. The dataset used for this analysis was the raw CoF and ES data collected with a sampling rate of 1 kHz.

4.3.1. Outlier detection of Starved-4 test

The outlier scores obtained using the five algorithms during the last run of Starved-4 are presented in Fig. 19. A sharp increase in outlier scores for both CoF and ES data was detected at around 1125 cycles, near the end of the run, by the FRR, IF, OCSVM, and LSTM algorithms. While the AE algorithm also indicated a sharp rise in outlier scores for the CoF data towards the end of the run, the outlier score for the ES data exhibited an increasing trend much earlier, starting at approximately 400 cycles.

During the Starved-4 test, a video was recorded to monitor the progression of wear on the plate. Fig. 20 (a), (b), and (c) show screenshots from the video captured during the final run of Starved-4. These screenshots correspond to different stages in the wear process: at 1130 cycles, just before debris became visible; at 1131 cycles, when debris first appeared near the stroke end; and at 1135 cycles, the final cycle of the run. After the test, an optical image of the wear scar at the stroke end was taken, clearly showing the accumulation of debris within the wear scar, as illustrated in Fig. 20 (d).

Based on the observation of wear evolution, the sharp increase in outlier scores for both CoF and ES, detected by the FRR, IF, OCSVM, and LSTM algorithms, occurred just before the visible accumulation of debris. This suggests that the rise in outlier scores was directly linked to the formation of debris. In contrast, the AE algorithm identified abnormal events much earlier, potentially corresponding to earlier stages of the wear process, such as mild oxidative wear and early debris formation. Given that the sample was lubricated with oil, the wear in

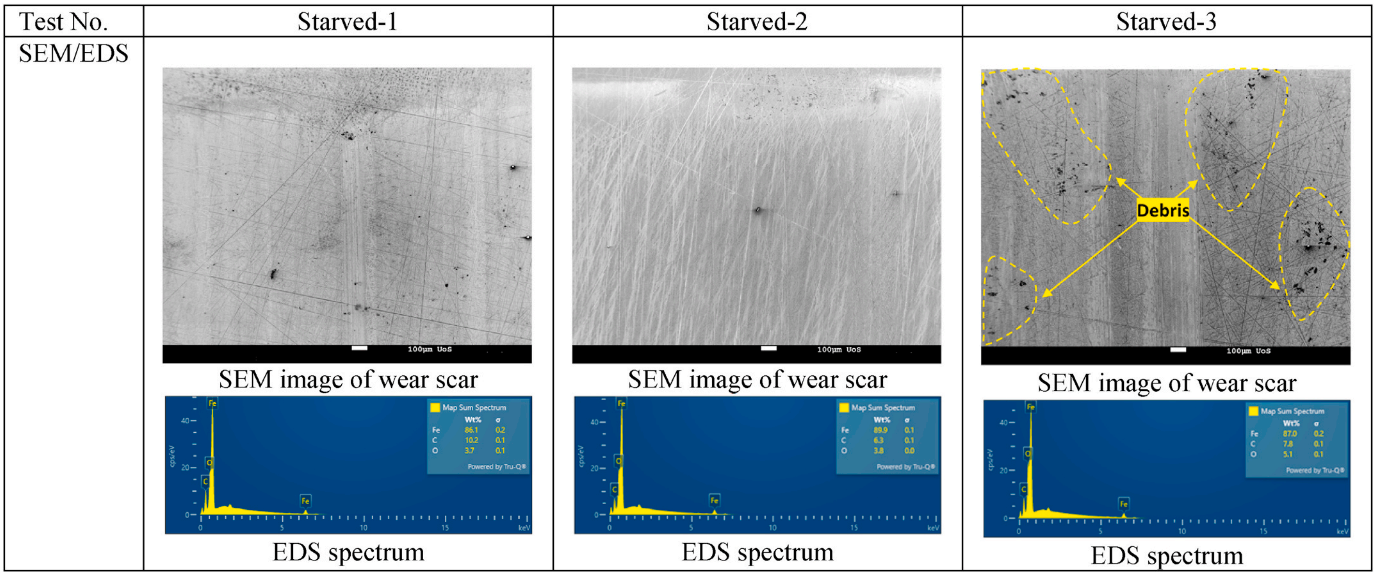

Fig. 18. SEM/EDS analysis of wear scar in starved tests.

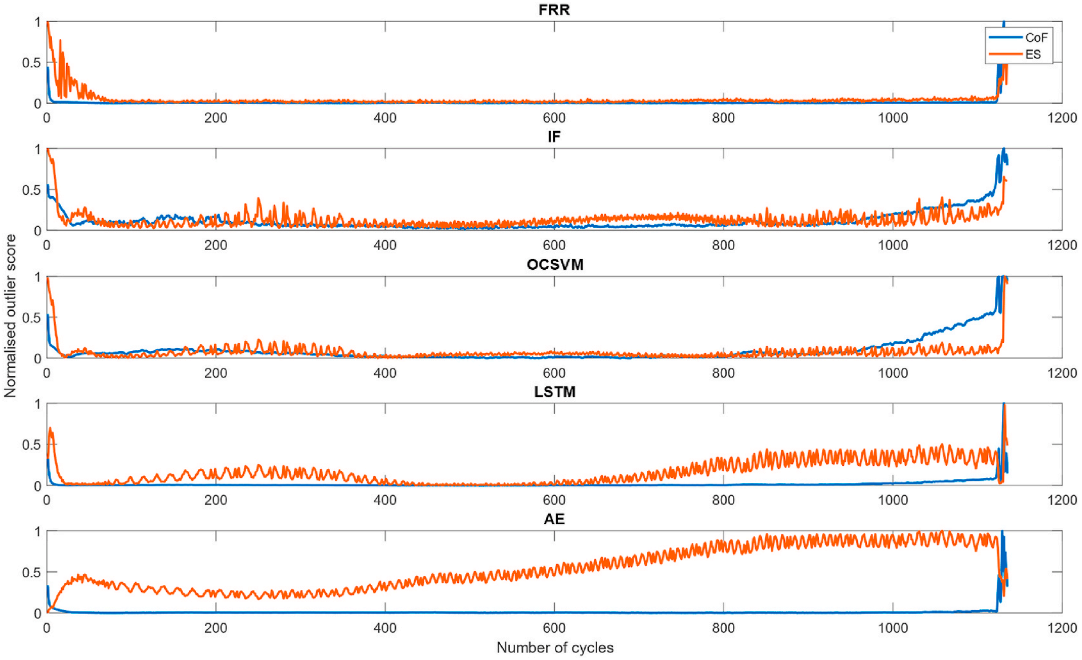

Fig. 19. Outlier scores versus number of cycles of the last run in Starved-4.

this test was relatively mild, resulting in small changes in surface charge. The AE algorithm demonstrated the highest sensitivity in detecting these early, subtle changes, making it particularly effective for identifying the onset of wear in such conditions.

4.3.2. Outlier score with Starved-3 test

The outlier scores for CoF and ES data during Starved-3 test calculated by the AE algorithm are shown in Fig. 21. No abnormal events were detected in either the CoF or ES data during the first four runs, likely due to the mild wear under the lubricated conditions. However, in the final run, fluctuations in the outlier scores for the ES data were observed, which may be attributed to the formation of oxide debris, as indicated by the SEM images presented in Fig. 18.

4.3.3. Outlier score with Dry-3 test

The outlier scores for the CoF and ES data calculated using the AE algorithm during Dry-3 test are shown in Fig. 22. In the first run, the outlier score of CoF fluctuated between 120 and 630 cycles (a total of 510 cycles) as highlighted in the black box. The number of cycles with fluctuating outlier scores in the subsequent four runs was also measured and is summarised in Table 4. The increase in the proportion (%) of the abrasive wear region was measured based on the optical images of the wear scars shown in Fig. 7 and is also listed in Table 4. An increase in the number of cycles with fluctuating outlier scores corresponds to a higher proportion of abrasive wear, suggesting that the outlier scores effectively revealed the progression of abrasive wear. By the fourth run, abrasive wear had covered the entire wear scar, and the progression rate slowed down, leading to a significant reduction in the number of cycles with fluctuating outlier scores. This suggests that the outlier algorithm is

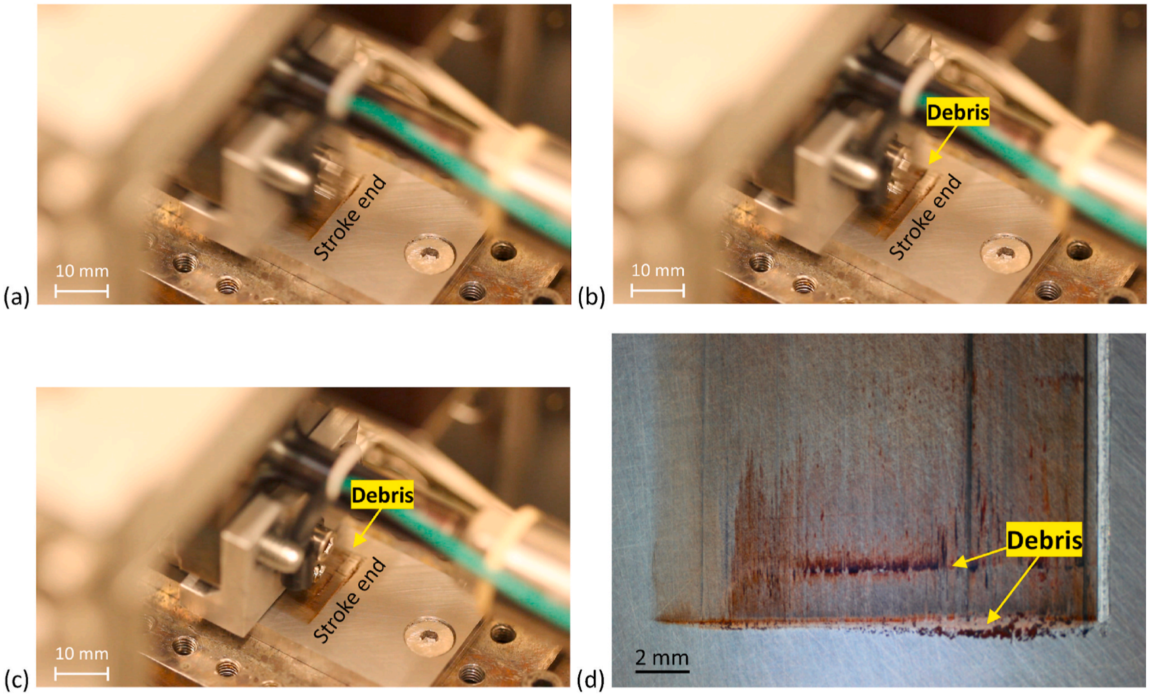

Fig. 20. Screenshot of the video taken at (a) 1130 cycles, (b) 1131 cycles, (c) 1135 cycles of the last run in Starved-4, and (d) the optical image taken at the end of the run.

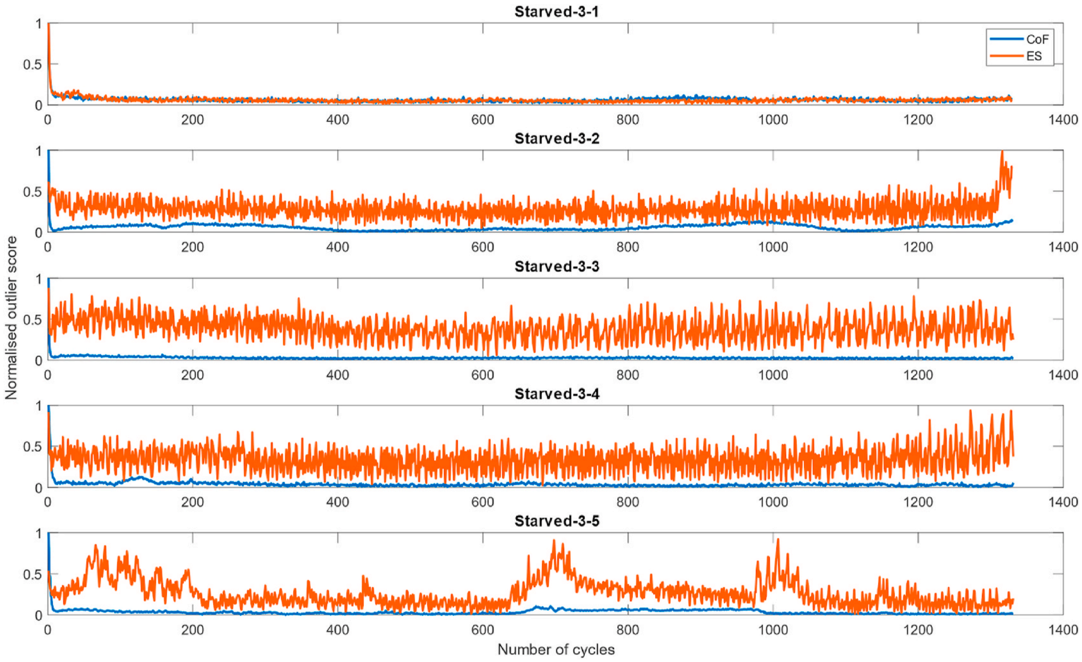

Fig. 21. Outlier scores of CoF and ES versus number of cycles of the five runs in Starved-3.

capable of detecting the signals associated with wear propagation, with lower scores associated with steady-state running.

The outlier detection of online electrostatic and friction data enables the real-time identification of early and mild wear mechanisms. The insights provided by electrostatic sensing enhance predictive digital twin technologies and contribute to early wear detection and predictive maintenance strategies.

5. Conclusions

This study investigated wear mechanisms occurring under dry and starved-lubricated conditions and the corresponding friction and electrostatic charge behaviours. The main findings are as follows:

- In this study, a bar electrostatic sensor was employed to detect the real-time charge, with the data used to explore its correlation with friction and investigate wear evolution. Additionally, an electrostatic array sensor was used to detect residual charge with higher

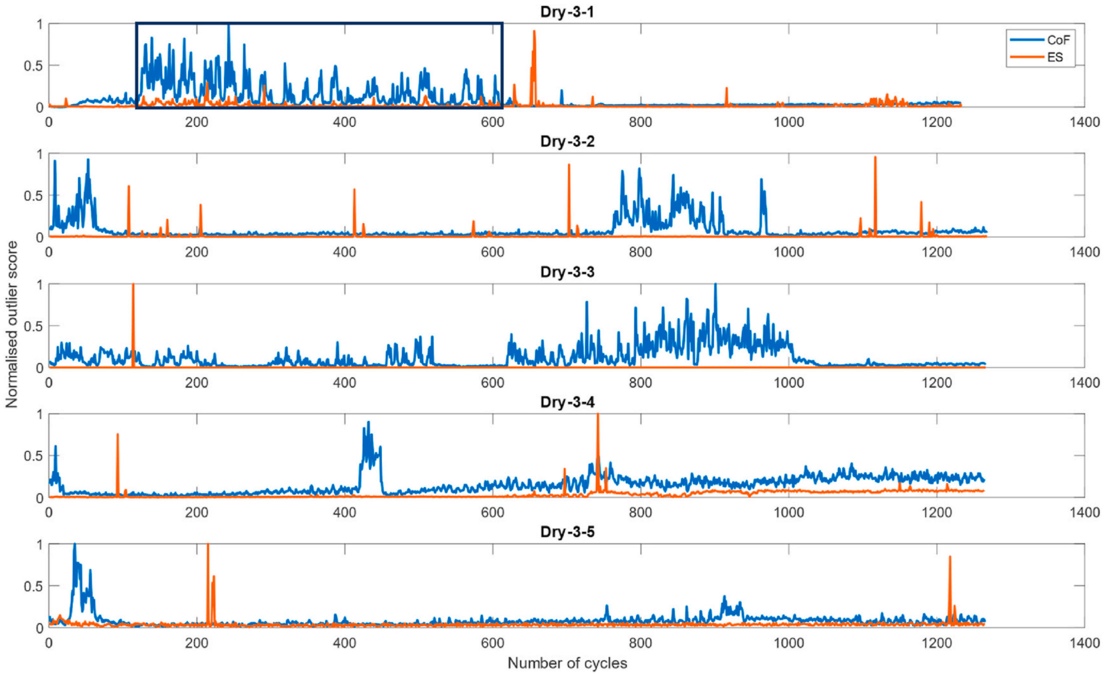

Fig. 22. Outlier scores of CoF and ES versus number of cycles of the five runs in Dry-3.

Table 4
Number of cycles with fluctuating outlier scores and increase in abrasive wear region in the five runs of Dry-3.

Run	Number of cycles with fluctuating outlier scores	Increase in abrasive wear region in proportion (%)
1	510	31.7
2	224	10.2
3	782	58.1
4	56	0
5	79	0

resolution, enabling the investigation of localised charge mechanisms and their relationships with wear mechanisms.

- In dry conditions, oxidational wear and abrasive wear were the dominant wear modes. Oxidational wear developed first, and as sliding continued, oxide debris accumulated and hardened, ploughing and surface and leading to the onset of abrasive wear. Oxidational wear was associated with a stable increase in the coefficient of friction (CoF), ranging from 0.4 to 0.6, while abrasive wear caused noisier CoF data.
- Positive electrostatic charge was detected during the dry tests, attributed to the presence of oxide films, which have a higher work function than steel. The relationship between friction and real-time charge was found to indicate the type of wear process. A linear relationship was observed during oxidational wear, whereas a nonlinear relationship was found during abrasive wear. EDS analysis revealed that in areas where oxidational wear was dominant, a localised higher oxygen percentage correlated with a higher electrostatic charge, showing a nearly linear relationship.
- In starved-lubricated conditions, the running-in process was characterised by a decreasing CoF and a reduction in surface roughness. Negative electrostatic charge was detected during these tests, potentially attributed to the lubricant type, reaction between the lubricant with the steel surface, and tribo-charging mechanism.
- Outlier detection algorithms were used to study the evolution of wear under dry and starved-lubricated conditions in-depth and showed potential in identifying evolution of wear. In dry tests, the algorithms found evidence of irregularities pointing to wear on the surface occurring. In starved-lubricated tests, they indicated subtle signs of damage from wear processes. This would indicate that the outlier detection has been successful in the early detection of wear propagation, before even very minor damage has occurred.

Electrostatic measurements are sensitive to environmental factors such as humidity and temperature, which can influence the identification of wear mechanisms. Additionally, interpreting charge signals in complex tribological systems with simultaneous wear mechanisms presents challenges. To address these issues, the effects of environmental factors on electrostatic charge behaviour such as generation and relaxation and their relationships to wear mechanisms will be investigated. Furthermore, electrostatic sensing will be integrated into a multi-modal sensing system to fully resolve sensor signals and their relationships to wear processes.

Declaration of competing interest

The authors declare that they have no known competing financial interests or personal relationships that could have appeared to influence the work reported in this paper.

Acknowledgements

The authors would like to thank the Engineering and Physical Sciences Research Council (EPSRC) funding: EP/S005463/1 Early detection of contact distress for enhanced performance monitoring and predictive inspection of machines for providing financial support for this work.

References

[1] G. Stachowiak, A. Batchelor, *Chapter 13: Corrosive and Oxidative Wear.* Engineering Tribology, Elsevier Butterworth-Heinemann, Burlington, MA, 2014.
[2] S. Lim, The relevance of wear-mechanism maps to mild-oxidational wear, Tribol. Int. 35 (11) (2002) 717–723.
[3] S. Morris, et al., Electrostatic charge monitoring of unlubricated sliding wear of a bearing steel, Wear 255 (1–6) (2003) 430–443.
[4] H. So, D. Yu, C. Chuang, Formation and wear mechanism of tribo-oxides and the regime of oxidational wear of steel, Wear 253 (9–10) (2002) 1004–1015.

[5] Q. Zhang, et al., Characteristics of oxidative wear and oxidative mildwear, Tribol. Int. 61 (2013) 214–223.

[6] E. Querlioz, et al., Experimental investigations on the contact fatigue life under starved conditions, Tribol. Int. 40 (10–12) (2007) 1619–1626.

[7] A. Kolivand, S. Li, Q. Zhang, Modeling on contact fatigue under starved lubrication condition, Meccanica 56 (2021) 211–225.

[8] C. Wen, et al., Starved lubrication analysis of angular contact ball bearing based on a multi-degree-of-freedom tribo-dynamic model, Friction 11 (8) (2023) 1395–1418.

[9] T. Liskiewicz, et al., Advances in sensing for real-time monitoring of tribological parameters, Tribol. Int. (2023) 108965.

[10] P. Lu, et al., Early wear detection and its significance for condition monitoring, Tribol. Int. 159 (2021) 106946.

[11] Z. Tian, et al., Charge pattern detection through electrostatic array sensing, Sensor Actuator Phys. 371 (2024) 115295.

[12] Y. Yan, et al., Electrostatic sensors–Their principles and applications, Measurement 169 (2021) 108506.

[13] H. Powrie, et al., Performance of an electrostatic oil monitoring system during an FZG gear scuffing test, in: Proceedings of the International Conference on Condition Monitoring, Coxmore Publishing Oxford, 1999.

[14] J. Booth, et al., Scuffing detection of TU3 cam–follower contacts by electrostatic charge condition monitoring, Tribol. Int. 43 (1–2) (2010) 113–128.

[15] H. Powrie, et al., Re-analysis of electrostatic wear-site sensor data from FZG gear scuffing tests, Wear 1 (2001) S2.

[16] O. Tasbaz, et al., Electrostatic monitoring of oil lubricated sliding point contacts for early detection of scuffing, Wear 230 (1) (1999) 86–97.

[17] P. Ramkumar, et al., The effect of diesel engine oil contamination on friction and wear, in: World Tribology Congress, 2005.

[18] J. Booth, et al., The feasibility of using electrostatic monitoring to identify diesel lubricant additives and soot contamination interactions by factorial analysis, Tribol. Int. 39 (12) (2006) 1564–1575.

[19] R. Penchaliah, et al., The effects of diesel contaminants on tribological performance on sliding steel on steel contacts, Proc. IME J. J. Eng. Tribol. 225 (8) (2011) 779–797.

[20] S. Chen, et al., Anomaly detection of the tapered roller bearings with statistical data-driven approaches, Insight-Non-Destruct Test Condition Monitor 52 (8) (2010) 428–436.

[21] M. Craig, et al., Advanced condition monitoring of tapered roller bearings, Part 1, Tribol. Int. 42 (11–12) (2009) 1846–1856.

[22] S. Chen, et al., Bearing Condition Monitoring Using Multiple Sensors and Integrated Data Fusion Techniques, 2008.

[23] S. Chen, et al., Use of artificial intelligence methods for advanced bearing health diagnostics and prognostics, in: 2008 IEEE Aerospace Conference, IEEE, 2008.

[24] S. Chen, et al., Wear detection of rolling element bearings using multiple-sensing technologies and mixture-model-based clustering method, Proc. Inst. Mech. Eng. O J. Risk Reliab. 222 (2) (2008) 207–218.

[25] Z. Tian, et al., Condition monitoring of pitting evolution using multiple sensing, in: Proceedings of the International Conference on Condition Monitoring and Asset Management, The British Institute of Non-Destructive Testing, 2023.

[26] T. Harvey, et al., Real-time monitoring of wear debris using electrostatic sensing techniques, Proc. IME J. J. Eng. Tribol. 221 (1) (2007) 27–40.

[27] T. Harvey, R. Wood, H. Powrie, Electrostatic wear monitoring of rolling element bearings, Wear 263 (7–12) (2007) 1492–1501.

[28] J. Sun, et al., Wear monitoring of bearing steel using electrostatic and acoustic emission techniques, Wear 259 (7–12) (2005) 1482–1489.

[29] L. Wang, et al., Electrostatic wear sensing of ceramic-steel lubricated contacts, in: Tribology Series, Elsevier, 2003, pp. 711–720.

[30] L. Wang, et al., Wear performance of oil lubricated silicon nitride sliding against various bearing steels, Wear 255 (1–6) (2003) 657–668.

[31] L. Wang, et al., Feasibility of using electrostatic monitoring for oil lubricated ceramic to steel sliding contacts, in: Tribology Series, Elsevier, 2003, pp. 625–635.

[32] T. Harvey, et al., Investigation of electrostatic charging mechanisms in oil lubricated tribo-contacts, Tribol. Int. 35 (9) (2002) 605–614.

[33] T. Harvey, et al., Effect of oil quality on electrostatic charge generation and transport, J. Electrost. 55 (1) (2002) 1–23.

[34] S. Morris, et al., Use of electrostatic charge monitoring for early detection of adhesive wear in oil lubricated contacts, J. Trib. 124 (2) (2002) 288–296.

[35] H. Powrie, L. Wang, R. Wood, Electrostatic monitoring of tribo-contacts: then and now, WCCM (2017) 2017.

[36] H. Lu, G. Hua, D. Li, Dependence of the mechanical behavior of alloys on their electron work function—an alternative parameter for materials design, Appl. Phys. Lett. (26) (2013) 103.

[37] J. Wang, et al., Explore the electron work function as a promising indicative parameter for supplementary clues towards tailoring of wear-resistant materials, Mater. Sci. Eng., A 669 (2016) 396–402.

[38] X. Huang, et al., Correlation between the wear resistance of Cu-Ni alloy and its electron work function, Phil. Mag. 95 (34) (2015) 3896–3909.

[39] V. Kumar, et al., Tribological properties of AZ31 alloy pre-deformed at low and high strain rates via the work function, Wear 414 (2018) 126–135.

[40] https://www.astmsteel.com/product/52100-bearing-steel-aisi/.

[41] https://www.tsmsteel.com/bo1-tool-steel.htm.

[42] F.T. Liu, K.M. Ting, Z.-H. Zhou, Isolation forest, in: 2008 Eighth Ieee International Conference on Data Mining, IEEE, 2008.

[43] B. Schölkopf, et al., Support Vector Method for Novelty Detection. Advances in Neural Information Processing Systems, 1999, p. 12.

[44] S. Hochreiter, J. Schmidhuber, Long short-term memory, Neural Comput. 9 (8) (1997) 1735–1780.

[45] G.E. Hinton, R.R. Salakhutdinov, Reducing the dimensionality of data with neural networks, Science 313 (5786) (2006) 504–507.

[46] T. Kasai, et al., Applications of a non-contacting Kelvin probe during sliding, Wear 225 (1999) 1186–1204.

[47] T. Quinn, Role of oxidation in the mild wear of steel, British J Appl Physics 13 (1) (1962) 33.

[48] P.J. Blau, On the nature of running-in, Tribol. Int. 38 (11–12) (2005) 1007–1012.

[49] T. Harvey, et al., Charging ability of pure hydrocarbons and lubricating oils, Tribol. Trans. 47 (2) (2004) 263–271.

[50] E.M. McCash, *Surface Chemistry*. (No Title), 2001.